



Complicated crustal deformation beneath the NE margin of the Tibetan plateau and its adjacent areas revealed by multi-station receiver-function gathering

Xiaoming Xu ^{a,b,c}, Fenglin Niu ^{b,d,*}, Zhifeng Ding ^a, Qifu Chen ^c

^a Institute of Geophysics, China Earthquake Administration, Beijing, China

^b Department of Earth, Environmental and Planetary Sciences, Rice University, Houston, TX, USA

^c Key Laboratory of Earth and Planetary Physics, Institute of Geology and Geophysics, Chinese Academy of Sciences, Beijing, China

^d State Key Laboratory of Petroleum Resource and Prospecting, and Unconventional Natural Gas Institute, China University of Petroleum at Beijing, Beijing, China

ARTICLE INFO

Article history:

Received 6 March 2018

Received in revised form 30 May 2018

Accepted 6 June 2018

Available online xxxx

Editor: A. Yin

Keywords:

cluster analysis
receiver function
crustal anisotropy
crustal deformation
NE Tibet
ChinaArray

ABSTRACT

We use a multi-station stacking method to analyze receiver function data recorded by a large-scale dense seismic array covering the northeastern (NE) margin of the Tibetan plateau and its adjacent regions to estimate crustal thickness (H), Vp/Vs ratio (κ) and crustal anisotropy (fast polarization direction φ and splitting time τ). For each station of the array, we gathered all the receiver functions recorded by the station and its nearby stations located inside a circle with a radius of 0.5° . We applied the $H-\kappa$ stacking technique and the joint inversion scheme to a total of 654 station clusters to measure the (H, κ) and (φ, τ), respectively. The measured Moho depth varies from a peak value of 67 km beneath the northern-central plateau to 39–45 km beneath the surrounding blocks in the northeast. The front of the depressed Moho beneath the plateau margin exhibits a complicated geometry, which suggests that when the Tibetan plateau encroached upon the surrounding terranes, the front expanded unevenly depending on the strength of the countering terranes. The thickened crust beneath the margin also has a very low Vp/Vs ratio, indicating that the crust is composed largely of felsic minerals. More than one third of the station clusters (221) have a splitting time significantly larger than 0.2 s. The average splitting times of the 221 measurements is 0.68 s, which is comparable to those measured from the SKS/SKKS (XKS) phases (0.94 s). The fast directions estimated from the Moho Ps and XKS phases recorded by the station clusters within the margin are very similar, and are also approximately parallel to the strikes of major faults, sutures and thrust fronts in the area. The low Vp/Vs ratio, together with the observed fast polarization directions from the Moho Ps and XKS phases, suggests that shortening of the entire lithosphere orthogonal to the compressional direction is likely the main cause for the observed crustal thickening occurring at the margin. We also found that the Moho Ps and XKS recorded by stations inside the western Hetao basin and the Yinchuan basin present very different anisotropy, which may suggest that the crust and mantle beneath the two basins have very different deformation patterns.

© 2018 Elsevier B.V. All rights reserved.

1. Introduction

The high topography and thick crust of the Tibetan plateau are generally believed to be caused by the continuous collision between the Indian plate and the Eurasian plate since ~ 50 Ma (e.g., Molnar and Tapponnier, 1975; Rowley, 1996; Yin and Harrison, 2000). The plateau has served as one of the natural laboratories in which modern thinking developed about plateau formation, the relationships between plate tectonics and mountain building, and

those between orogenesis, climate, erosion and uplift. Besides the Indian plate in the south, the Tibetan plateau is also bounded by several continental blocks with very little to no deformation, such as the Tarim basin to the northwest, the Alxa block to the north, the Ordos block to the northeast and the Sichuan basin to the east (Fig. 1). The NE margin of the Tibetan plateau is a tectonic transition zone between the uplifted Tibetan plateau and the stable Alxa block and the Ordos block, and plays an important role in its growing toward the northeast.

Several models have been proposed to explain the geodynamic mechanism of the crustal thickening and deformation of the Tibetan plateau. Zuba et al. (2016) provides a nice summary on

* Corresponding author.

E-mail address: niu@rice.edu (F. Niu).

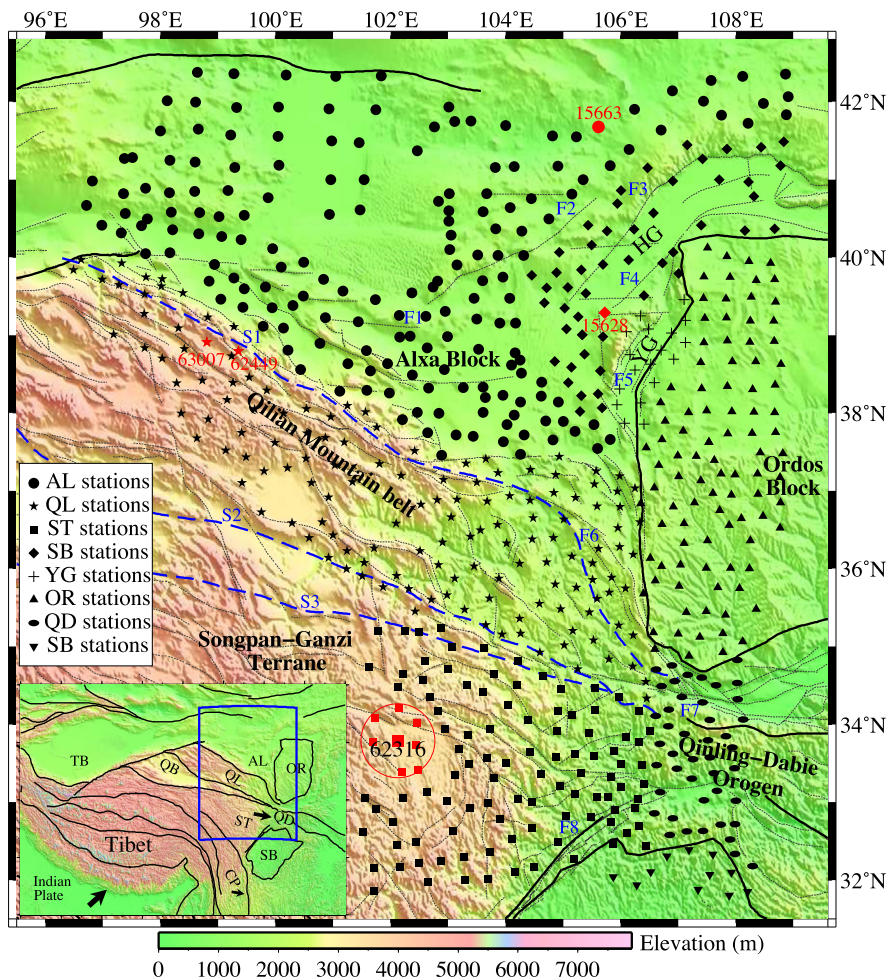


Fig. 1. Topographic map showing the seismic stations used in this study, and the tectonic units, main faults (after Wu et al., 2016). Stations located in different blocks are indicated with different symbols. Inset shows the sketch tectonic setting of the Tibetan plateau and its adjacent blocks. The blue rectangular shows the location of the study region. The black thick arrowhead indicates the absolute plate motion (APM) direction from GSRM v2.1 model (Kreemer et al., 2014). The bold black lines mark the boundaries of the major tectonic units: OR (the Ordos Block), AL (the Alxa Block), QD (the Qinling-Dabie Orogen), QL (the Qilian Mountain belt), ST (the Songpan-Ganzi Terrane), SB (the Sichuan Basin), CP (the Chuandian Plateau), QB (the Qaidam Basin), TB (the Tarim Basin). The two Cenozoic Hetao and Yinchuan grabens located at the northwestern corner of the Ordos block are labeled with HG and YG, respectively. S1: the North Qilian Suture; S2: the South Qilian Suture; S3: the Ayimaqin-Kunlun Suture. F1: the Taohualashan-Ayouqi fault; F2: the Yabulaishan Fault; F3: the Bayanwulashan-Langshan Fault; F4: the Dengkou-Benjing Fault; F5: the Huanghe Fault; F6: the Haiyuan Fault; F7: the Qinling Fault; F8: the Longmenshan Fault. Black triangles represent stations of the second phase deployment of the ChinArray project. The red squares in the red circle at the low-left corner are considered as the cluster of station 62316 for multi-station gathering.

these various models and how they specifically apply to the northern and northeastern margin of the plateau. Among these models, two end-member models, the whole-lithosphere-shortening model (England and Houseman, 1986; Dewey et al., 1988; Meyer et al., 1998) and the middle-to-lower crustal flow model (Royden et al., 1997, 2008; Clark and Royden, 2000), are well discussed in the solid earth science community. In the first model, deformation is accommodated coherently across the entire lithosphere, while in the second model deformation along the plateau margins is accomplished through the intrusion of the middle and lower crustal material from the central plateau to the margins. The two deformation models predict very different velocity and anisotropy structure of the lithosphere beneath the margins. While these two models focus on crustal thickening and uplift, they do not address the development of the large strike-slip fault system in the margin. Tapponnier et al. (2001) proposed an intracontinental subduction model, in which multiple subduction of the Asian lithosphere occurred in coupled with lateral extrusion of different tectonic blocks along the major strike-slip faults. As this block extrusion model does not offer specifics on the deformation within the blocks and involves intracontinental subductions that require deep seismic

imaging technique to resolve, hence the primary focus of this study is to constrain the above two end-member models.

Recently, many seismologists have investigated the crustal and upper mantle structure with different types of techniques and data in order to diagnose the dominant mechanism responsible for the deformation along the margins of the plateau. The issue is, however, still not fully resolved. Ambient noise tomographic images (Yao et al., 2008; Yang et al., 2012; Chen et al., 2014) show continuous lower S-wave velocity anomalies in the middle and lower crust depths beneath the SE margin of the plateau, a scenario seems to be consistent with the middle-to-lower crust flow model. Receiver function studies, on the other hands, show a moderate to low crustal V_p/V_s ratio beneath the NE margin, together with a crustal azimuthal anisotropy that is more consistent with the whole crustal shortening model (Pan and Niu, 2011; Li et al., 2015; Ye et al., 2015, 2016; Wang et al., 2016, 2017a; Huang et al., 2017). Many other seismic studies, however, found that crust and upper mantle structures beneath these margins are far more complicated, and are difficult to be explained by one of these end-member mechanisms. For example, the distribution of the low-velocity anomalies beneath the NE margin is rather com-

plicated and could be discontinuous, and thus the low-velocity anomalies cannot be explained by a simple middle-to-lower crustal flow (Li et al., 2014; Liu et al., 2014; Zheng et al., 2016).

Seismic anisotropy study can greatly improve our understanding of lithospheric deformation due to its close relationship with the subsurface stress and/or strain field (Crampin and Lovell, 1991; Silver, 1996). While the whole-lithosphere-shortening model suggests that deformation inside the crust and lithospheric mantle should be coherent, the mid-lower crustal flow model, on the other hand, implies that the flow-induced fabrics in the middle and lower crust could be significantly different from those in the mantle. Knowledge on the vertical distribution of seismic anisotropy thus can offer potential answers to the underlying physical processes responsible for the observed deformation. Both body wave (e.g., Zhao et al., 2017) and surface wave (e.g., Pandey et al., 2015) data have been used to estimate azimuthal seismic anisotropy inside the crust and mantle lithosphere beneath the Tibetan plateau and its surrounding regions. Seismic anisotropy of the upper mantle is commonly measured by waveform splitting of the core phases, SKS, SKKS, and PKS, which are referred to as XKS hereafter. Li et al. (2011) and Chang et al. (2017) investigated deformation field in the lithosphere beneath the NE margin of the Tibetan plateau using seismic anisotropy derived from XKS waveform splitting. Since the observed seismic anisotropy from XKS could, in principle, be located anywhere along the S-wave ray path from the core–mantle boundary (CMB) to the surface at the receiver side, it is thus impossible to use XKS to determine the deformation pattern inside the crust and mantle separately.

S waves from local earthquakes occurring in the upper to middle crust have been employed to study azimuthal seismic anisotropy in the upper crust beneath the NE Tibetan plateau (Zhang et al., 2012a; Qian et al., 2017). Seismic anisotropy in the upper crust is generally attributed to the stress-induced alignment of fractures and cracks, and is usually featured by small splitting times (<0.1 s) as compared to those from XKS data (~1.0 s). Measurements of seismic anisotropy inside the lower crust thus become crucial for bridging the gap between surface GPS data, shear-waves splitting data derived from local S waves and teleseismic XKS phases. In principle, the P-to-S converted phase at the Moho (P_s) is an ideal phase to study crustal anisotropy. However, the Moho P_s phase recorded by individual seismograms is of too low amplitude to permit robust shear-wave splitting measurements like XKS. Liu and Niu (2012) developed a comprehensive technique that utilizes radial and transverse receiver functions to estimate crustal anisotropy. Sun et al. (2012) further proposed to add a harmonic analysis in the processing which aims to further argument the measurement. Wang et al. (2016) employed the method to measure crustal anisotropy beneath the NE margin of the plateau. They found that the Moho P_s and the XKS show roughly the same fast polarization directions, which they argue for a vertically coherent deformation within the lithosphere beneath the margin. The comprehensive analysis package proposed by Liu and Niu (2012) and Sun et al. (2012), however, only works for stations that are underlain by a relatively flat and sharp Moho and possess good quality receiver functions with a good backazimuthal coverage. As such, robust measurement of crustal anisotropy can be made only from very few seismic stations.

We noticed that the methods of Liu and Niu (2012) and Sun et al. (2012) were designed for analyzing single station data. In this study, we extend this single-station based receiver function technique to receiver functions gathered from multiple stations that are closely located. We applied this technique to teleseismic data recorded by a large-scale dense array of broadband seismographs recently being deployed at the NE margin of the Tibetan plateau and its adjacent regions (Fig. 1). Based on the multi-station gathered receiver function data, we estimated the Moho depth, V_p/V_s

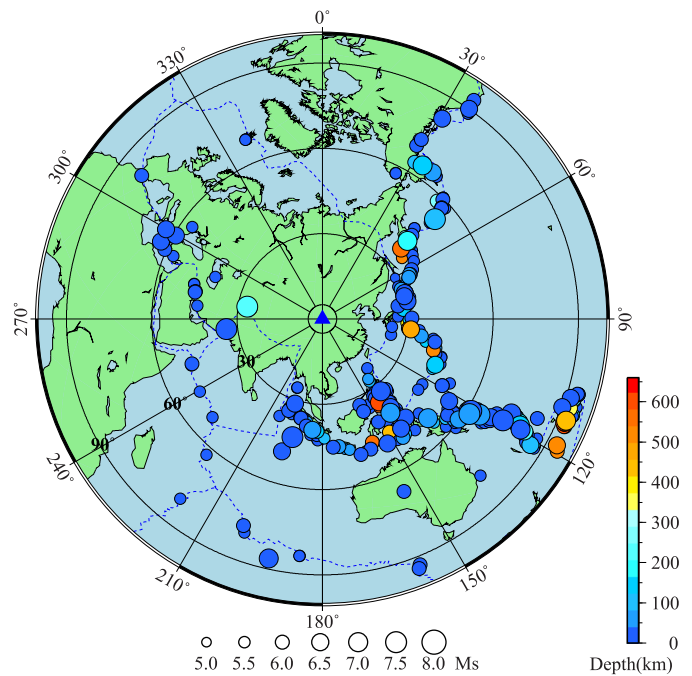


Fig. 2. Locations of 439 earthquakes used in this study. Note that although some events are located inside the 30° and outside the 90° circle, all the seismograms we used have an epicentral distance between 30° and 90° .

ratio and crustal anisotropy beneath the array. In general, the measurements turned out to be much more stable and robust since a larger number of receiver functions were used in the analyses as compared to the single-station approach. In particular, the number of robust measurements of crustal anisotropy increases significantly with the multi-station gathering due to the large amount of receiver functions and the broad coverage in backazimuth of teleseismic events. In the following sections, we first describe the data and the modified method, and then present a new model of the thickness, average V_p/V_s ratio and azimuthal anisotropy of the crust beneath the Tibetan plateau and its adjacent areas. They are followed by a discussion of some implications of the deformation mechanism of the NE margin and the regional tectonics of the study area.

2. Data and analysis

2.1. ChinArray phase II deployment

We used waveform data recorded by the second phase deployment of the ChinArray project, which plans to roll over mainland China with a transportable array consisting of ~800 broadband seismographs with a station spacing of ~30–40 km. The second phase of the ChinArray deployment covers an area of $10^\circ \times 10^\circ$ centered at the NE margin of the Tibetan plateau and its adjacent regions from October 2013 to April 2016. Each seismograph is equipped with a Guralp CMG-3ESP seismometer and a Reftek 130 data logger. We selected a total of 654 stations that have high quality three component recordings. To calculate the receiver functions, we used a total of 439 earthquakes with a magnitude greater than 5.0 and an epicentral distance between 30° and 90° . As shown in Fig. 2, a large portion of the teleseismic events are located inside the western Pacific subduction zone and the Java trench with a back azimuth between 30° and 210° . We also have many earthquakes coming from other back azimuths; therefore the overall coverage in backazimuth is reasonably good, which seems to be also true for the distance coverage (Fig. 2).

To generate receiver functions for the three-component recordings of a teleseismic event, we first need to rotate the two horizontal components into the radial (R) and transverse (T) directions based on the great arc raypaths connecting the events and stations. It is important to employ the true orientation of the two horizontal components, which might be different from the north and east directions due to misalignment, for conducting the rotation. Therefore we first used the P wave particle motions of teleseismic events to determine the true sensor orientation for each station with the method proposed by Niu and Li (2011).

2.2. Receiver functions and multi-station gathering

After rotating the horizontal components into *R* and *T*, we further projected *R* and *T* components to the principal directions (longitudinal, *P*, and in-plane transverse, *SV*) estimated from the covariance matrix in order to minimize the P wave energy in the receiver function. We then computed the receiver functions with these two components, as did by many other studies (Vinnik, 1977; Niu and Kawakatsu, 1998; Niu et al., 2007).

We used the “water-level” deconvolution technique (Clayton and Wiggins, 1976; Ammon, 1991), which is designed in the frequency domain, to generate receiver functions:

$$RF(\omega) = \frac{V(\omega) \cdot P^*(\omega)}{\max\{|P(\omega)|^2, \gamma \cdot |P_{\max}(\omega)|^2\}} e^{-\left(\frac{\omega}{2\alpha}\right)^2}. \quad (1)$$

Here, γ and α are two constants that define the “water level” and the corner frequency of the Gaussian low pass filter. We set them to be 0.01 and 1.5, respectively. $P(\omega)$ and $V(\omega)$ are the spectra of the P and SV components taken from a 200 s time window (50 s before and 150 s after the P wave). We used the method of Chen et al. (2010) to remove outliers. We selected a total of 151,341 receiver functions from the 654 stations, with a station average of ~231 receiver functions.

Seismic array processing technique has been used to detect weak signals and image Earth’s structure for 50 yr (Rost and Thomas, 2009). By stacking individual station records of the array, we expect the noise to be canceled out while signals to remain, leading to a significant increase of the signal-to-noise ratio (SNR). Here the SNR is defined as the ratio of average amplitude computed from a signal window, 2–10 s after the direct P and a noise window 2–4 s before the direct P, respectively. We drew inspiration from seismic array processing technique and then proposed the multi-station gathering method to process the receiver function data in this work. The dense seismic array deployed in the NE Tibetan plateau and its adjacent regions offers an excellent opportunity to perform the processing of receiver functions using multi-station gathering method. We first considered a reference station and its surrounding stations in a circled with a radius of 0.5° as a station cluster, such as the station cluster 62316 located at lower left corner shown in Fig. 1. For each teleseismic event, we first formed a cluster receiver function by summing all the receiver functions recorded by the stations inside the cluster using the *N*th-root stacking technique (Muirhead, 1968; Kawakatsu and Niu, 1994). To take account the distance effect on the Moho Ps arrival, we employed the ray parameter based stacking method developed by Chen and Niu (2013). Let $x_j(t + \delta t_j)$ represents the receiver function of *j*th station in the cluster, δt_j is the distance related correction, which is zero for the reference station. The cluster receiver function, $r(t)$, which is the *N*th-root stack of the gathered individual receiver functions, is given by

$$r(t) = y(t) |y(t)|^{N-1}, \quad (2)$$

where

$$y(t) = \frac{1}{M} \sum_{j=1}^M \text{sign}(x_j(t + \delta t_j)) |x_j(t + \delta t_j)|^{1/N}. \quad (3)$$

Here *M* is the total number of stations within a cluster, and *N* was set to 2. As shown in the later examples, the uncorrelated noise is greatly suppressed, whereas the coherent phases are significantly amplified in the cluster receiver functions, as compared to single-station receiver functions.

2.3. Depth stacking and *H*– κ analysis

For each station, we applied the multi-station gathering technique to obtain cluster receiver functions. We then adopted the two-step analysis following Niu et al. (2007) to estimate the crustal thickness and the average *V_p/V_s* ratio beneath each cluster centered at the reference station. This includes a first step of depth stacking to determine the initial depth of the Moho using the Moho Ps phase alone, followed by a refined *H*– κ analysis to estimate the final Moho depth and *V_p/V_s* ratio that has the largest stacking value of the Moho Ps and the multiples.

To compute the initial depth, we first converted the time-domain receiver functions to depth-domain P-to-S conversion coefficient functions. Here we made an assumption that receiver function data comprise primarily of P to S conversions at various depths. For an assumed conversion depth, *d*, we computed the P-to-S conversion time by ray tracing with a modified iasp91 velocity model (Kennett and Engdahl, 1991) that has a crustal thickness of *d*. We then stacked the depth-domain receiver functions using the same *N*th-root stacking technique with *N* = 2. We searched *d* from 0 to 100 km with an interval of 1 km and considered the depth with maximum stacking amplitude as the initial crustal thickness. Fig. 3a and 3b show examples of the depth stacks of receiver functions gathered at the station 62316 and cluster 62316, respectively. A clear P to S conversion peak can be found at ~54 km in Fig. 3a and ~57 km in Fig. 3b, respectively.

We continued to use the phase notation of *npms* introduced by Niu et al. (2007) to perform the *H*– κ analysis. For a hypothetic crustal thickness, *H*, and *V_p/V_s* ratio, κ , we first computed the relative arrival times of the Moho Ps and the two crustal multiples with respect to the direct *P* wave, which are denoted as *t*₁, *t*₂, and *t*₃, respectively. We then stacked the three arrival windows based on their polarities:

$$s(H, \kappa) = \frac{c(\kappa)}{K} \sum_{i=1}^K \{w_1 r_i(t_1) + w_2 r_i(t_2) - w_3 r_i(t_3)\}. \quad (4)$$

Here *K* is the total number of receiver functions at a given station or cluster, $r_i(t)$ represents the amplitude of the *i*th receiver function at time *t*. w_1 , w_2 , and w_3 are the weights of the three time windows, which are assigned to 0.5, 0.25, and 0.25, respectively. $c(\kappa)$ is a coherence index of the three phases, which is introduced by Niu et al. (2007) to reduce the trade off between *H* and κ . We also used three combinations in the *H*– κ analysis: (1) including all three phases, (2) using 0p1s and 1p2s phases, and (3) 0p1s and 2p1s phases to ensure robust measurements. Meanwhile, κ was varied in the range of 1.5 to 2.0 with an increment of 0.001 and *H* was searched within ±20 km of the initial depth derived from the depth stacking. *H* and κ were determined when the summed amplitude, $s(H, \kappa)$, reached its maximum. In Fig. 3c and 3d, we show the results of *H*– κ analysis based on station 62316 and cluster 62316, which give an estimate of (*H*, κ) being (56.0 km, 1.678) and (54.4 km, 1.727), respectively.

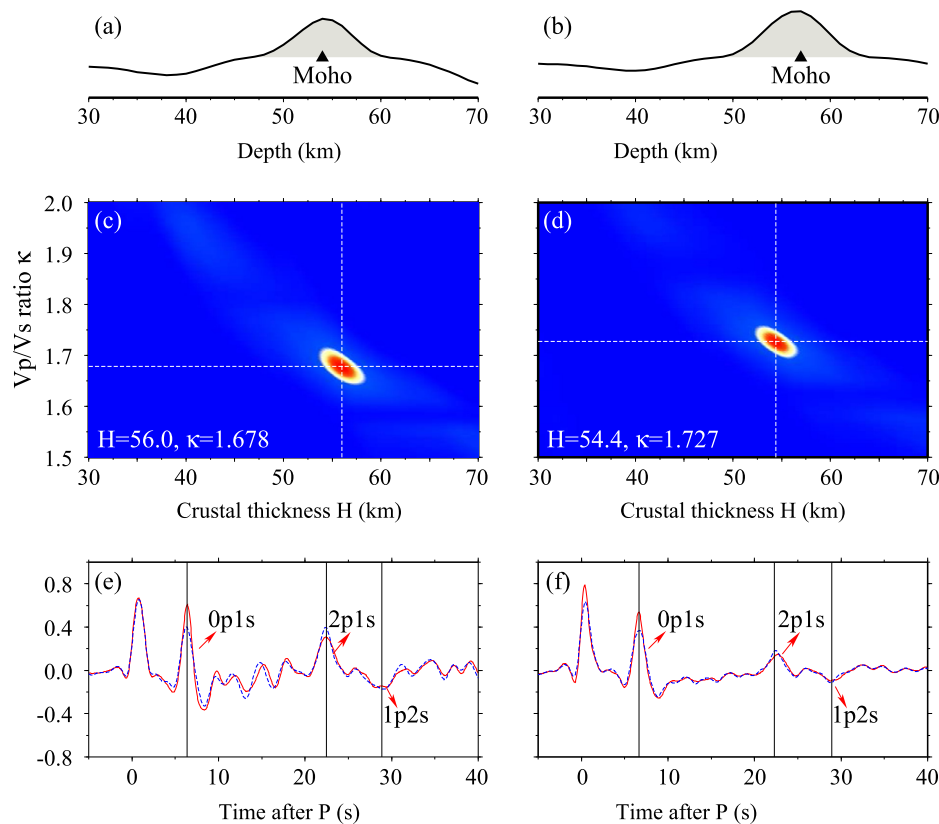


Fig. 3. (a) and (b) are the stacked receiver functions after the time-to-depth conversion of station 62316 and cluster 62316 respectively. The maximum peak marked by black triangle indicates the initial Moho depth. (c) and (d) are the results of $H-\kappa$ analysis at station 62316 and cluster 62316. The cross white lines indicate the location of the peak amplitude. (e) and (f) show the time domain stacked receiver functions with the Ps slowness (red solid line) and the 2p1s slowness (blue dashed line). Note that amplitude of the phases is larger when they are stacked with the correct slowness. (For interpretation of the colors in the figure(s), the reader is referred to the web version of this article.)

2.4. Moveout correction and harmonic analysis of the Moho Ps

In general, the relative arrival time of the Ps phase has a negative distance moveout due to its negative slowness with respect to the direct P wave. We calculated the moveout and make corrections for each station cluster using the estimates of crustal thickness and V_p/V_s ratio derived from the above $H-\kappa$ analysis. After corrections, all the cluster receiver functions are expected to have a Moho Ps arrival time equivalent to the one with an epicentral distance of 60° and a source depth of 0 km. For the comprehensive analysis of crustal anisotropy, we employed R - and T -component based receiver functions, which are normalized with the peak amplitude of the P wave. After the moveout correction and normalization, we investigated the R and T receiver functions as a function of back azimuth to study the systematic variations in the peak Ps arrival time of the R receiver functions and polarity changes of the T receiver functions.

The Moho Ps arrival time can be caused by inhomogeneous crustal structures, various types of anisotropy and scattering (Levin and Park, 1997; Savage, 1998; Shiomu and Park, 2008). For example, a dipping Moho or an anisotropic crustal layer with an inclined symmetry axis can result in a harmonic degree-1 back azimuthal variation, while small-scale heterogeneities in the crust and Moho topography can act as seismic scatterers, leading to high order ($n > 2$) degree variations along back azimuth direction. On the other hand, azimuthal S-wave anisotropy with a horizontal symmetric axis can register a degree-2 back azimuthal variation in the Ps arrival time. We employed the method proposed by Sun et al. (2012) to analyze the back-azimuthal variations, which calculates the normalized maximum amplitude ($A_{n,\max}$), maximum energy ($E_{n,\max}$), and minimum total residual ($R_{n,\min}$) between each re-

ceiver function and the stacked receiver function that are summed along a harmonic moveout with a degree varying from 1 to 8. In Fig. 4a and 4b, we show the station-based and cluster-based receiver functions of station 62316 that are plotted in the order of back azimuth. Fig. 4c shows the results of harmonic analysis with the cluster receiver functions, which shows clear peaks of the $A_{n,\max}$, $E_{n,\max}$ and $1/R_{n,\min}$ at degree 2.

2.5. Estimate of crustal anisotropy

We applied the method of Liu and Niu (2012) to estimate crustal anisotropy beneath each hypothetic cluster. The analysis includes computing three individual objective functions (IOFs) and one joint objective function (JOF), and performing a statistical analysis on the robustness of the estimated anisotropy. The three IOFs are (1) peak energy of the stacked R receiver function, (2) the cross correlation of the R receiver functions, and (3) the total energy of transverse receiver functions, and the JOF is the average of the three IOFs. The statistical analysis evaluates a signal or noise window by examining whether it increases steadily with the number of stacking.

In Fig. 5, we show the analysis of crustal anisotropy at the station cluster 62316. The φ and τ estimated from the three IOFs and the JOF are shown in Fig. 5a–c and Fig. 5d, respectively. All the four measurements agree well with each other. We further evaluate the robustness of the estimated φ and τ by comparing the SNRs of the Ps on the R and T components before and after the correction of crustal anisotropy, which are shown in open and filled symbols in Fig. 5e and 5f, respectively. The SNR computed from stacked T receiver functions with a polarity correction shows a steady increase with $S^{1/2}$ (open squares in Fig. 5e). Without the polarity correc-

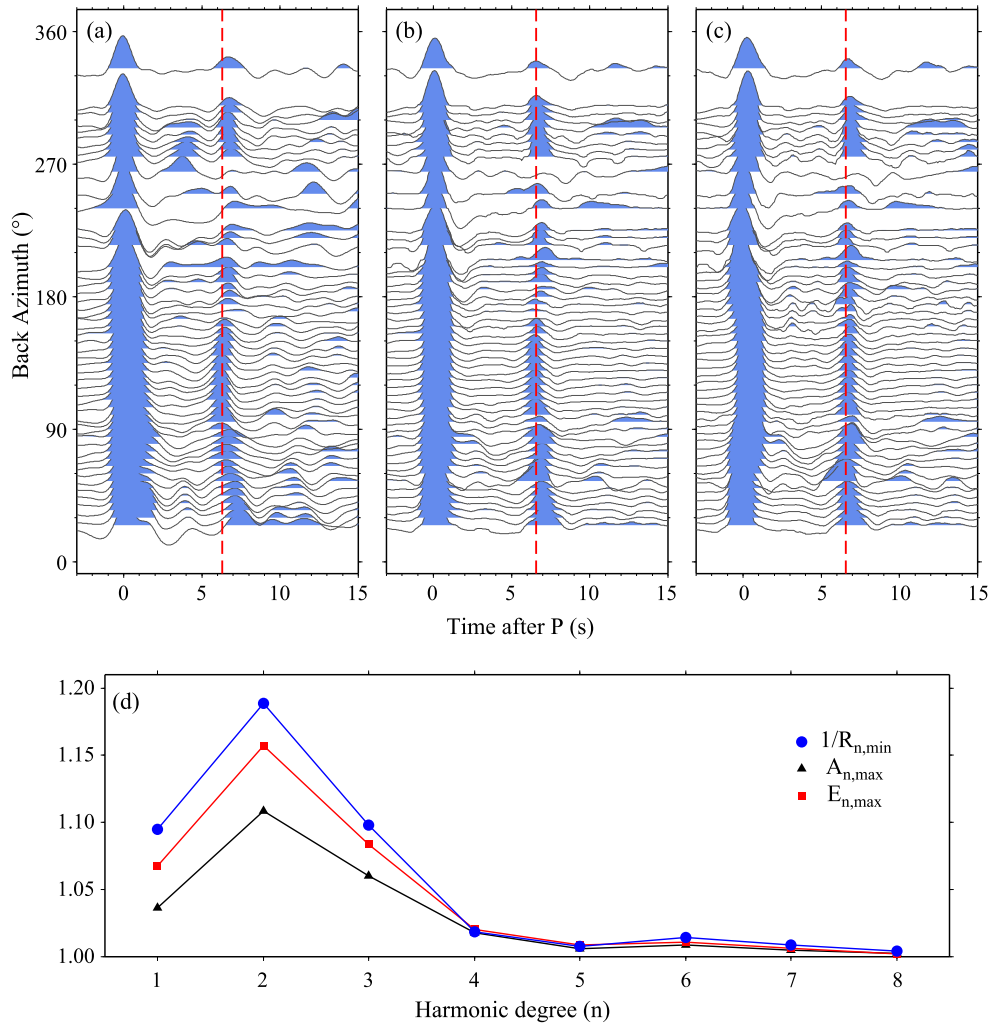


Fig. 4. Radial receiver functions are plotted as a function of back azimuth at the station 62316 (a) and cluster 62316 (b). For comparison, (c) shows the same sets of radial receiver functions after the crustal anisotropy being corrected. The red dashed lines denote the average arrival time of the Moho Ps phase. The result of harmonic analysis of cluster 62316 is shown in (d). The reciprocal of the minimum residual, the maximum value of peak amplitude and total energy are plotted as a function of the harmonic degree.

tion, the SNR increases much more slowly (open circles in Fig. 5e), probably due to uneven distribution in backazimuth of the data. On the other hand, once the crustal anisotropy is corrected, SNR remains low regardless of whether a polarity correction is made (solid squares in Fig. 5e) or not (solid circles in Fig. 5e). Meanwhile, SNR computed from the stacked R receiver functions after correcting crustal anisotropy (filled triangles in Fig. 5f) increases steadily with $S^{1/2}$, and generally appears to be larger than those uncorrected (open triangles in Fig. 5f).

For comparison, we also show the R receiver functions after the correction of crustal anisotropy at the station cluster 62316 in Fig. 4c. The back-azimuthal variation shown in Fig. 4b before the corrections almost disappeared here, suggesting that azimuthal anisotropy inside the crust does seem to be the cause of the arrival time variations of the Moho Ps phase.

3. Results

3.1. Moho depth and V_p/V_s ratio

We conducted the $H-\kappa$ analysis at all the stations with the single station and cluster based receiver function data. The measured Moho depth from the two sets of receiver functions are shown in Fig. S1a and S1b, respectively, while the estimated V_p/V_s ratios

are plotted in Fig. S2a and S2b. The measurements are also listed in Table S1, which is organized by grouping stations in the following tectonic units: the Alxa block (AL), the Hetao graben (HG), the Ordos block (OR), the Qinling–Dabie orogen (QD), the Qilian Mountain belt (QL), the Sichuan basin (SB), the Songpan–Ganzi terrane (ST) and the Yinchuan graben (YG). The average crustal thickness, V_p/V_s ratio, and crustal anisotropy are listed in Table 1, together with other parameters.

In order to further show the lateral variations of Moho depth and V_p/V_s ratio beneath the study area, we employed the inversion scheme of Niu et al. (2007) to interpolate the measurements at 654 clusters into 2475 meshed grids of $0.25^\circ \times 0.25^\circ$. The inverted Moho depth and V_p/V_s ratio are shown in Fig. 6a and 6b, respectively. Overall, the Moho in the study area exhibits significant topography, which also shows a good spatial correlation with tectonic blocks in the area (Fig. 6). We note that the measured Moho depth varies from ~ 39 km at the station cluster 15663 (Fig. 1) in the northern Alxa block to ~ 67 km (Fig. 1) at the station cluster 63007 located in the western Qilian Mountain belt. The Ordos block appears to have the thinnest crust (43.7 km) while the Qilian Shan thrust belt possesses the thickest crust (53.7 km) in the study area, which is comparable to the previous results (Chen et al., 2005; Pan and Niu, 2011; Yue et al., 2012; Wang et al., 2016). Meanwhile, the lowest and highest V_p/V_s ra-

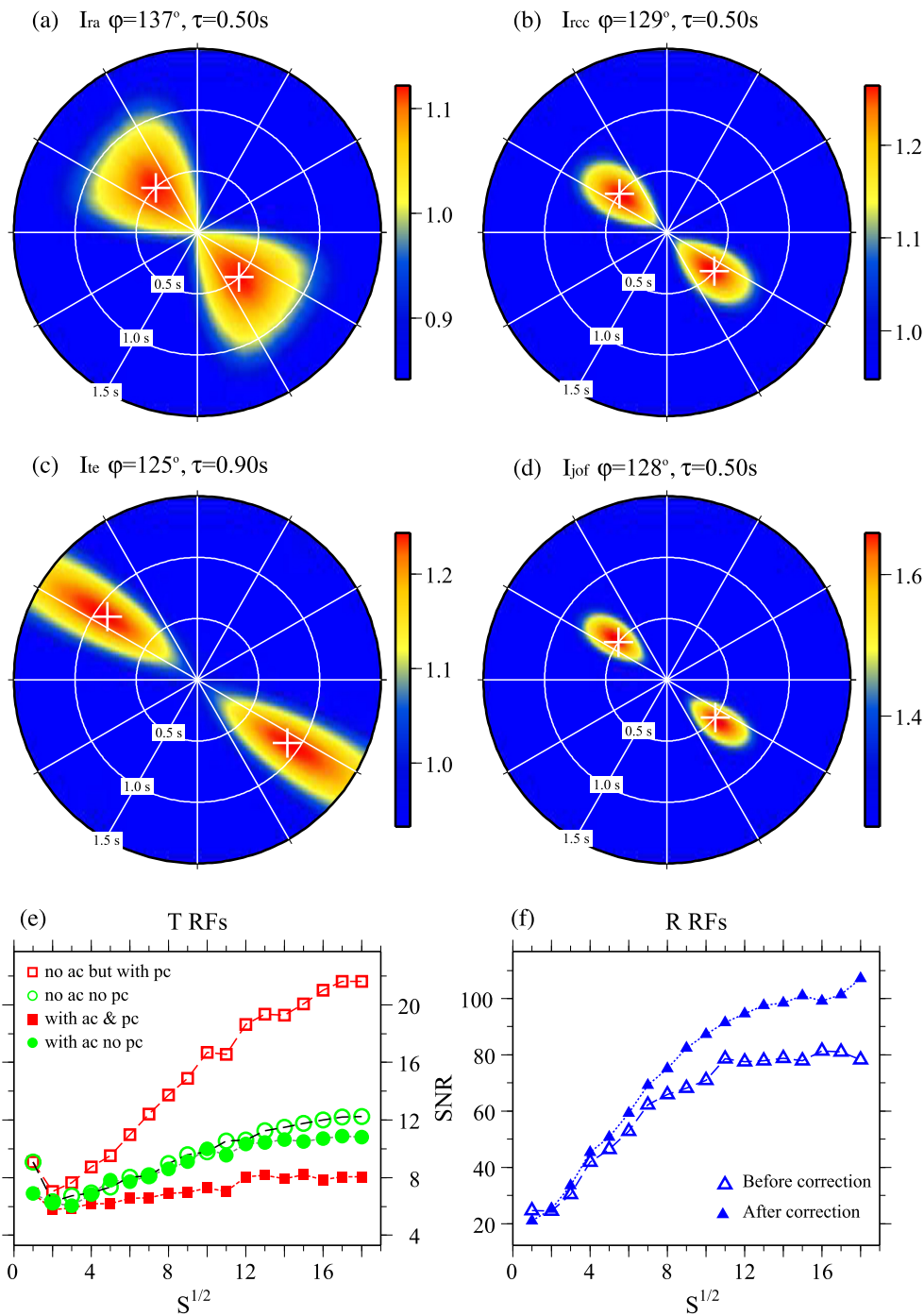


Fig. 5. Measurements of crustal anisotropy from the joint analysis with multi-component receiver function data at cluster 62316. (a), (b) and (c) show three individual methods to estimate seismic anisotropy: (1) radial energy maximization with a cosine moveout correction; (2) radial correlation coefficient maximization; (3) transverse energy minimization. (d) is the joint solution. (φ, τ) are searched in the range of $0\text{--}360^\circ$ and $0\text{--}1.5$ s with an increment of 1° and 0.02 s, respectively. White plus marks the measured (φ, τ) where the objective functions reach to maximum. (e) and (f) show the calculated SNRs of stacked receiver function data as a function of the square root of the subsample numbers, $S^{1/2}$. Open and filled symbols in (e) and (f) indicate SNR calculated from stacks of receiver functions before and after the removal of seismic anisotropy measured by the joint receiver function. More specifically, opened squares shown in (e) indicate stacks from T receiver functions without anisotropy correction but with polarity correction, while opened circles are from T receiver function with no corrections of anisotropy and polarity. Filled squares and circles represent stacks after correction of anisotropy, and with and without polarity correction, respectively.

tios are, respectively, observed at the station cluster 62449 (1.607) located at the Qilian Mountain and the station cluster 15628 (1.879) inside the Hetao graben (Fig. 1). The Qilian Mountain belt seems to have the lowest average Vp/Vs ratio (1.724) while the Hetao graben possesses the highest Vp/Vs ratio (1.777) in the study region.

In general, the observed crustal thickness and Vp/Vs ratio are in good agreement with the results of previous studies (Pan

and Niu, 2011; Xu et al., 2013; Wang et al., 2017a). The lateral variations of the crustal thickness and Vp/Vs ratio, however, show much more details than previous studies that used much less seismic stations. One interesting feature shown in the Moho depth map is that the front of the thickened crust appears to have a zigzag geometry (green dotted line in Fig. 6a), suggesting that crustal thickening did not occur uniformly across its front.

Table 1
Average properties of the crust beneath major blocks.

Tectonic units	H (km)	κ	φ ($^{\circ}$)	τ (s)	$\Delta\varphi_X$ ($^{\circ}$)	$\Delta\tau_X$ (s)	$\Delta\varphi_G$ ($^{\circ}$)	$\Delta\varphi_A$ ($^{\circ}$)
AL	46.4	1.740	101.5	0.7	21.1	0.3	-18.1	1.4
OR	43.7	1.766	90.2	0.6	20.8	0.1	13.1	12.7
HG	45.4	1.777	59.4	0.7	80.5	0.2	36.5	42.5
YG	44.0	1.755	42.2	0.8	85.0	0.2	50.6	60.0
QD	45.3	1.725	105.5	0.5	-11.8	0.4	-0.9	-2.7
QL	53.7	1.724	118.7	0.7	0.9	0.4	-45.2	-18.9
SB	46.7	1.748	-	-	-	-	-	-
ST	49.5	1.733	120.4	0.7	-10.6	0.2	-29.5	-19.8

H , κ , φ and τ are the average crustal thickness, V_p/V_s ratio, Pms fast polarization direction and splitting time. $\Delta\varphi_X$, $\Delta\varphi_G$ and $\Delta\varphi_A$ are the directional residuals between the XKS splitting (Chang et al., 2017), GPS velocity (Zhao et al., 2015) and APM (Kreemer et al., 2014) and the Moho Ps phase splitting. The “-” symbol indicates null measurement. $\Delta\tau_X$ (s) is the difference of splitting time measured between the XKS and Pms. Major blocks are: AL, the Alxa block; OR, the Ordos block; HG, the Hetao Graben; YG, the Yinchuan Graben; QD, the Qinling–Dabie Orogen; QL, the Qilian Mountain belt; SB, the Sichuan Basin; ST, the Songpan–Ganzi Terrane.

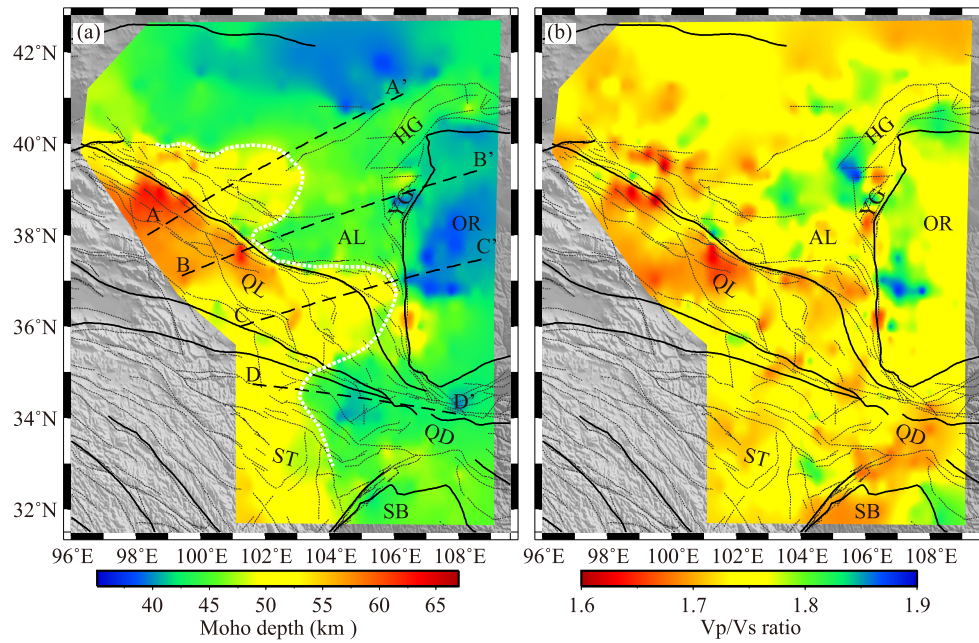


Fig. 6. Maps of Moho depth (a) and V_p/V_s ratio (b) estimated from observations at 654 station clusters. The abbreviations of tectonic blocks are defined in the caption of Fig. 1. The dashed white line indicates the front of the depressed Moho beneath the plateau margin, which is roughly a smoothed line with a Moho depth of ~ 48 km.

Fig. 7 shows four depth sections that extend from the plateau to the neighboring blocks at different parts of the front. The northernmost section AA' (Fig. 6a) runs across the Qilian Mountain belt to the Alxa block through the Northern Qilian suture (S1), where we found that the Moho jumps rapidly from ~ 61 km to ~ 53 km (Fig. 7a). It then gradually shallows to ~ 50 km beneath the Taohualashan–Ayoubi fault (F1) and further shoals to ~ 45 km beneath the northern Alxa. The BB' line (Fig. 6a) runs across the Northern Qilian suture (S1) through a convex front (Fig. 6a). Here the Moho shallows as much as ~ 12 km across the suture, and stays nearly flat under the Alxa block (Fig. 7b). Moho depth changes along the CC' line appear to be more gradual, and there seems no noticeable changes across the Northern Qilian suture (Fig. 7c), which defines the surficial front of the plateau. The DD' line runs from the plateau to the Qinling–Dabie mountain range, and also shows a rather gradually changing Moho (Fig. 7d). Overall, the crust is not thickened so much beneath this part of the Songpan–Ganzi terrane.

The measured V_p/V_s ratio also shows significant variations in the study area (Fig. 6b). The western Ordos, western Hetao graben and areas west to the Hetao and Yinchuan grabens have the largest V_p/V_s ratio in the study area, with an average V_p/V_s ratio greater than 1.8. The Qilian Mountain belt, the Songpan–Ganzi terrane and

Qinling–Dabie orogen, on the other hand, have a very low V_p/V_s ratio, generally below 1.732 (Table 1). We also noticed that the observed V_p/V_s ratio appears to anti-correlate with crustal thickness; regions with a thick crust tend to have a low V_p/V_s ratio, which was also observed in North America by Lowry and Pérez-Gussinyé (2011).

3.2. Crustal anisotropy

Although we had measurements of crustal anisotropy at all the station clusters, which are listed in Table S1, we only chose station clusters with a degree-2 harmonic variation, which leads to 221 measurements of the crustal anisotropy from the total 654 station clusters. The estimates of harmonic degree and splitting parameters, as well as the results of the statistical analysis are listed in Table S1. We used “-” to indicate stations or station clusters that are lack of enough back azimuthal coverage, and “X” to denote unstable and anomalous measurements (measured splitting time, $\tau > 1.5$ s), respectively. For stations or station clusters with $\tau < 0.2$ s, we marked them with “Null”. These measurements are mainly found in the cratonic Alxa and Ordos blocks (Fig. S3). In addition, “0” in the harmonic degree column means that the harmonic degree space has a broad distribution, which may suggest

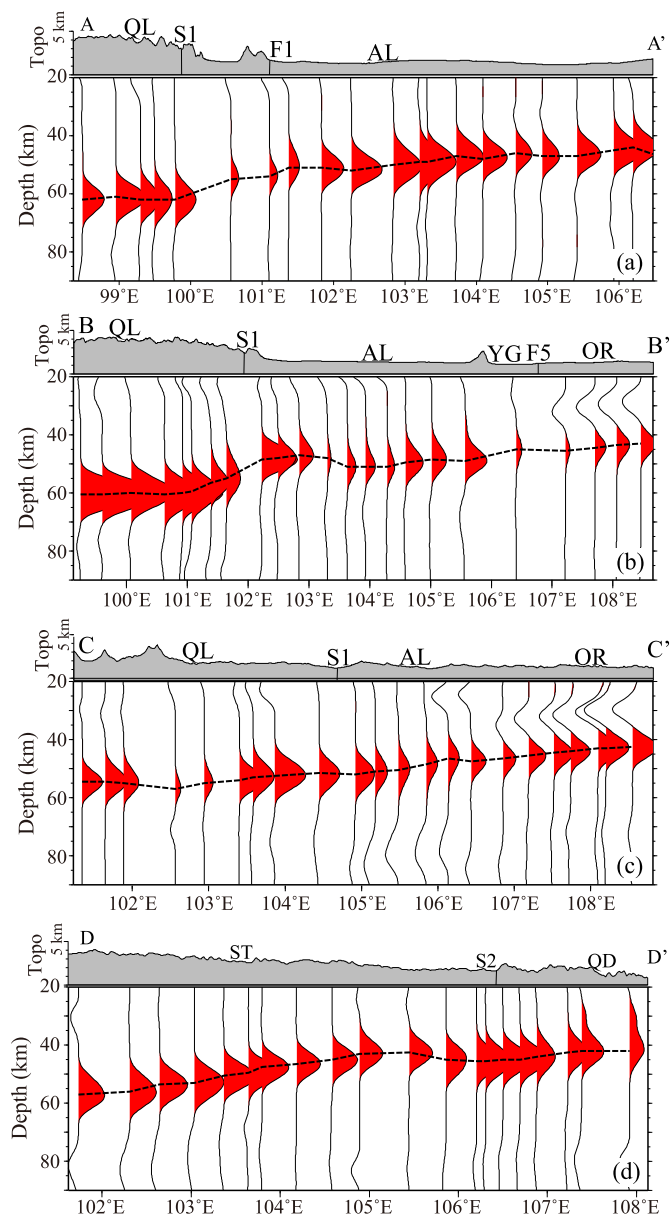


Fig. 7. Profiles of receiver functions in depth domain along lines of AA', BB', CC' and DD' shown in Fig. 6a. The abbreviations are defined in the caption of Fig. 1.

a complicated crustal structure beneath these stations or station clusters. A robust measurement is defined when the harmonic analysis possesses a degree $n = 2$ and receiver functions before and after the correction of the estimated azimuthal anisotropy are distinctly different. We take station cluster 62316 as an example to exhibit the crustal anisotropy beneath the Songpan–Ganzi terrane (Fig. 1). The estimated polarization direction and delay time at this station cluster are 128° and 0.5 s, respectively.

Comparing with the number of crustal anisotropy measurements from station clusters and single stations, we found that the number of the robust estimates from multi-station stack is 221 (Fig. S3b), which is much more than the 89 measurements derived from the single-station gather (Fig. S3a) due to the improved SNR and back azimuthal coverage. Fig. 8 shows the fast polarization direction and splitting time of the Moho Ps at the 221 station clusters (red lines), together with those measured from the XKS phase (blue lines, Chang et al., 2017) as well as the GPS motion directions (green arrow, Zhao et al., 2015) and the absolute plate motion (thick black vectors, Kreemer et al., 2014). The fast polar-

ization direction measured from most of station clusters shows a NW–SE direction, roughly parallel to the strike of surface structures, for example, the strike of the Qilian thrust front. In general, the fast polarization directions show a good agreement with those measured from XKS data (blue line in Fig. 8). Stations located inside the Hetao and Yinchuan Grabens and their surrounding areas (marked by white ellipse in Fig. 8a), however, show a distinct NE–SW fast polarization direction, which is nearly perpendicular to the rest of the stations as well as to those derived from the XKS splitting data. We also notice that the fast polarization directions measured in the northwestern part of the study area show substantial differences between the Ps and XKS splitting data with an average up to $\sim 21^\circ$ as shown in Table 1. As uncertainties in the fast direction measurements can be as large as 10° , therefore we would like to leave the investigation of these potential differences and their causes for future studies.

The average splitting time of the 221 measurements is 0.68 s, which is consistent with those measured from the permanent stations in the area (Wang et al., 2016), but is larger than those estimated from individual receiver functions (Xie et al., 2017). We attribute this difference to the large uncertainties in the measurements of crustal anisotropy using individual receiver functions, in which the Moho Ps has very low SNR. While the large splitting times measured at many station clusters indicate that the crust underneath them are highly deformed, we also noticed that many stations located at the Ordos block and the Alax block showed very weak to no seismic anisotropy.

We also compared our Moho Ps measurements with those from the XKS data, which is summarized in Table 1. We found that the two datasets show roughly similar fast polarization directions at five tectonic units, QL, ST, QD, AL, and OR, but very different ones at the other two blocks, the Hetao (HG) and Yinchuan (YG) grabens. For the five blocks with similar fast polarization directions, the Moho Ps splitting times are only slightly lower than those measured from XKS. In other words, nearly 70–80% of the XKS splitting times are originated inside the crust.

4. Discussion

Moho depth is a key parameter in characterizing the crustal structure and deformation (Zandt and Ammon, 1995). The large lateral variations of the Moho depth (Fig. 6a) indicate the complexity of the crustal structure beneath the NE Tibetan plateau and its adjacent regions. The average Moho depth shallows from 53.7 km beneath the Qilian Mountain belt to 46.4 km in the Alxa block in the north, to 43.7 km beneath the Ordos block in the northeast, and to 45.3 km beneath the Qinling–Dabie orogen in the east (Table 1). This means that the Moho beneath this area roughly dips toward southwest, which was also reported by previous studies (Pan and Niu, 2011; Xu et al., 2013; Wang et al., 2017a). In general, the observed Moho depth appears to be correlated with surface topography (Fig. 7), which means that surface topography is roughly supported by crustal buoyancy.

One new feature revealed by this study is the zigzag front of the depressed Moho, which shows some correlation, but does not match exactly with the surface front of the plateau. When the Tibetan plateau encroached upon the surrounding terranes, the front expanded unevenly depending on the strength of the encountering terranes. This might explain the observed zigzag front of the Moho. A recent P-wave traveltome tomographic study (Guo et al., 2017) shows that the southwest Alxa area next to the convex front of the depressed Moho has a distinct high velocity mantle lithosphere extending to ~ 250 km. Zhang et al. (2012b) also found that this part of the Alxa block has a very thick lithosphere based on S-wave receiver function data. All these results suggest that the southwestern Alxa has a strong lithosphere such

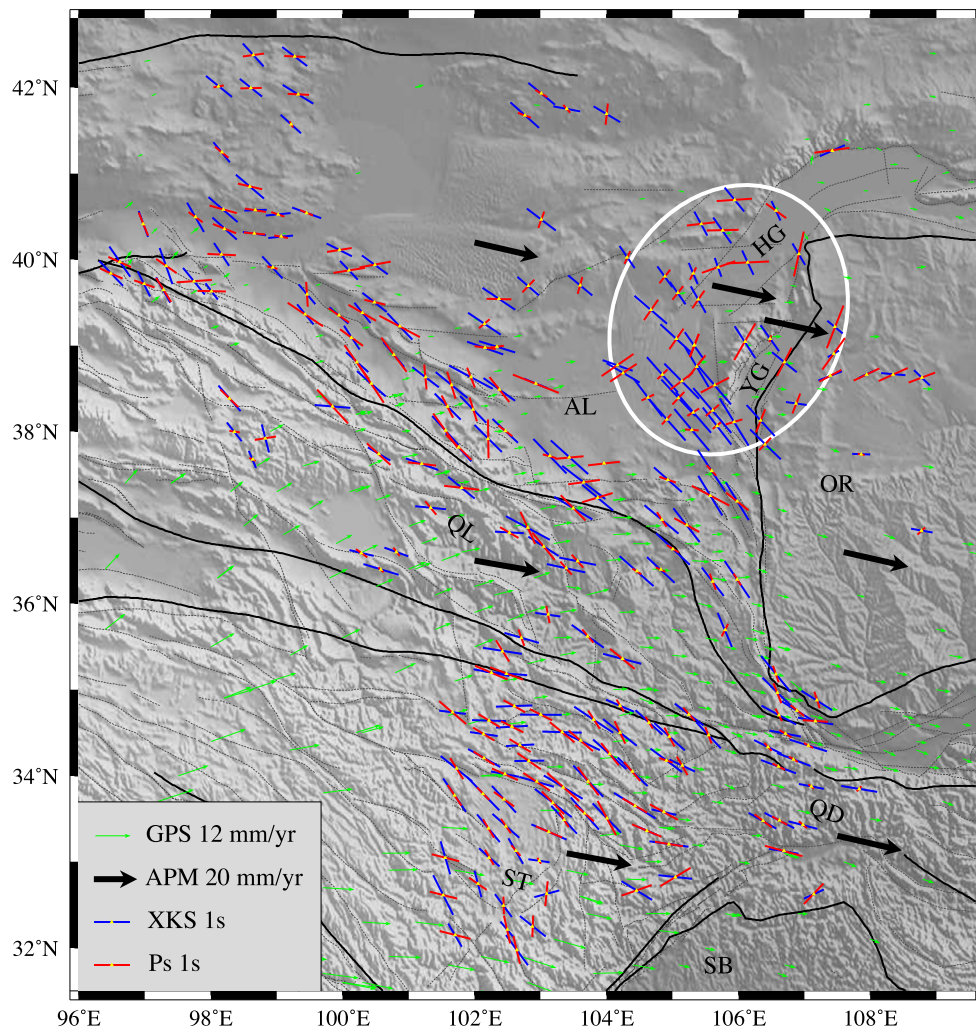


Fig. 8. The two anisotropic parameters, (φ , τ), measured from the Moho Ps and XKS phases (Chang et al., 2017) are shown in red and blue bar lines, respectively. The orientation and length of the bar lines represent the fast-axis direction and the amount of splitting, respectively. For comparison, the GPS velocity (Zhao et al., 2015) and the absolute plate motion (APM) direction of the GSRM v2.1 model (Kreemer et al., 2014) are also indicated with thin green and thick black arrows, respectively. White solid ellipse outlines the anomalous region where the fast polarization directions measured from the Moho Ps and XKS are nearly perpendicular to each other.

that it hardly deforms in spite of the strong compression from the Qilian thrust belt, which leads to the formation of a convex front in the depressed Moho. Meanwhile, the lower crust and upper mantle beneath the Qilian Mountain belt are featured by lower P- and S-wave velocity (Guo et al., 2017; Li et al., 2017; Wang et al., 2017b). The area is also featured by high heat flow greater than 60 mW/m² (Hu et al., 2000; Tao and Shen, 2008). All these suggest that the orogen has a thin and weak lithosphere that provides the mechanical basis for whole lithosphere shortening.

We further argue that whole lithosphere shortening has been occurring and is responsible for crustal thickening in the NE margin of the Tibetan plateau based on the observed crustal thickness, average V_p/V_s ratio and azimuthal seismic anisotropy. The first evidence comes from the observed low V_p/V_s ratio beneath the Qilian mountain range and the Songpan–Ganzi terrane. Laboratory data suggested that the V_p/V_s ratio is related to rock types and can be used to constrain the bulk average composition of the crust (Christensen, 1996). When temperature is far below the rock solidus, the V_p/V_s ratio varies very little with temperature, but is particularly sensitive to the composition. More specifically, the V_p/V_s ratio is good indicator of silica content when it is less than 1.74 (Erdman et al., 2013). Mafic rocks tend to have high V_p/V_s ratio as compared to felsic rocks. An increase of plagioclase content and a decrease of quartz content usually give rise to the increase

of the V_p/V_s ratio, and the high V_p/V_s ratios (>1.87) indicate the existence of partial crustal melting (Tarkov and Vavakin, 1982; Christensen, 1996; Owens and Zandt, 1997). The observed low V_p/V_s ratio is thus inconsistent with the lower crustal flow model. If the crust is thickened by an injection of mafic lower crustal material, then the average composition of the thickened crust is expected to be mafic, leading to a high V_p/V_s ratio. Furthermore, the low V_p/V_s ratio suggests that crust is likely rich in quartz and hence is weaker than more mafic crust (Lowry and Pérez-Gussinyé, 2011), which implies that the crust beneath the Qilian Mountain range and the Songpan–Ganzi terrane is easier deformation vertically. Pan and Niu (2011) further argued that the systematic low V_p/V_s ratio beneath the Songpan–Ganzi terrane is due to its tectonic origin. The Songpan–Ganzi terrane was an accretionary wedge with felsic composition before the Qiangtang block collided with the Tarim–North China block (Watson et al., 1987; Wu et al., 2016).

The second evidence is from seismic anisotropy data. Measurements of seismic anisotropy in the crust are also conducive to understanding crustal deformation. In general, seismic anisotropy in the upper crust is attributed to stress-induced alignment of cracks (Crampin and Peacock, 2008), while anything below is more likely to be caused by strain-induced lattice preferred orientation of minerals (Meissner et al., 2002). Sherrington et al. (2004) found

that seismic anisotropy in the middle to lower crust can reach as high as ~14%. As mentioned above, seismic anisotropy of the whole crust can be constrained by measuring the Moho Ps splitting as the vertically propagation S wave is confined within the crust. Results of the crustal anisotropy estimated from receiver functions (McNamara and Owens, 1993; Sherrington et al., 2004) suggested that most of the observed anisotropy is derived from the middle-to-lower crust. Zhang et al. (2012a) and Qian et al. (2017) computed azimuthal anisotropy using shear wave splitting from local earthquakes occurring in the upper crust of the NE Tibetan plateau, and obtained an average delay time of 6 ms/km in the upper crust, which means that the total splitting time accumulated in a 15 km upper crust is less than 0.1 s, much smaller than the observed Moho Ps splitting time of 0.68 s. Therefore, seismic anisotropy determined from the Moho Ps here is likely to be resulted primarily from the middle-to-lower crust.

We noticed that fast polarization directions measured from Moho Ps and XKS are quite similar, which align dominantly along WNW–ESE in the Qilian Mountain belt and Songpan–Ganzi terrane (Fig. 8), and the XKS splitting times are only slightly larger than those measured from the Moho Ps. These observations suggest that the lithosphere beneath the NE margin of the Tibetan plateau deforms coherently along depth with a compressional direction of SSW–NNE, which is roughly parallel to surface GPS motion direction (green arrows in Fig. 8). The small difference in the splitting time between the two phases suggests that crustal anisotropy is likely the primary contributor to the observed XKS splitting. It also implies that the mantle lithosphere beneath the area is relatively thin (Zhang et al., 2012b; Ye et al., 2015; Guo et al., 2017; Li et al., 2017; Wang et al., 2017b). For example, Zhang et al. (2012b) found that the lithosphere is ~125–135 km thick beneath the northeastern Songpan–Ganzi block and ~170–200 km thick beneath the Alxa and Ordos blocks. Li et al. (2011) measured shear wave splitting with XKS phase from earthquakes coming from a wide range of back azimuths and found that a simple uniform anisotropic model can explain most of the measurements. This also provides an indirect evidence for a vertically coherent deformation beneath the margin. On the other hand, if crustal thickening is caused by an inflow of middle-to-lower crustal material from the central Tibet, then the fast polarization is expected to align with the flow direction, which is roughly along the NE direction in this area, and obviously is not supported by the Moho Ps data.

One distinct area in Fig. 8 is the western Hetao and Yinchuan graben located at the northwest corner of the Ordos block where the fast polarization directions measured from the Moho Ps phase and XKS are nearly perpendicular to each other (white solid ellipse). It is generally thought that the Cenozoic grabens around the Ordos block were developed due to the northeastward escaping of the Tibetan plateau and the interaction between the Tibetan plateau and its surrounding blocks (Zhang et al., 1998). The two grabens have a rift axis aligning roughly along the NE–SW direction, which is more or less the fast direction of the observed crust anisotropy in this region. In general, extensional normal faults form parallel to the axis rift and exist only inside the crust. Earthquake focal mechanism data indicates a transtensional motion along these faults (Rao et al., 2018), suggesting that the observed crustal anisotropy is most likely caused by the simple shear motion along these faults. On the other hand, the extension that led to the development of the grabens is along the NW–SE direction, which aligns well with the fast polarization direction of the XKS phases. Therefore the XKS splitting is most likely caused by the alignment of olivine crystals of the mantle lithosphere.

5. Conclusions

In this study, we measured crustal thickness (H), V_p/V_s ratio (κ) and crustal anisotropy (fast polarization direction φ and splitting time τ) using receiver function data recorded by a large-scale dense array that covered the NE margin of the Tibetan plateau and its surrounding areas. We developed a method that gathers receiver functions within a station cluster in performing the H – κ and anisotropy analyses, which allowed us to obtain better estimates of the four parameters than regular receiver-function analysis does. Based on the four measured parameters (H , κ , φ and τ), we reached on the following conclusions: (1) The Moho beneath NE margin of the Tibetan plateau is depressed by 10–20 km with a zigzag front roughly coincides, but does not exactly follow the surficial front of the margin. The complicated front is likely caused by different strength of the encountered terranes as the margin expands; (2) Whole lithosphere shortening along the compressional direction is likely the primary cause of the observed crustal thickening occurring at the margin; (3) Deformation within the crust and mantle lithosphere beneath the Cenozoic Hetao and the Yinchuan grabens appears to be distinctly different, which may reflect the transtensional faulting inside the crust and extensional rift in the mantle.

Acknowledgements

We thank the Data Management Center of China Seismic Array at Institute of Geophysics, China Earthquake Administration (ChinArray DMC, <https://doi.org/10.12001/ChinArray.Data>) for providing the waveform data. We also thank Dr. Andrew V. Zuzva and another anonymous reviewer for their constructive comments and suggestions, which significantly improved the quality of this paper. This work was supported by National Key R&D Program of China (2017YFC1500303), the National Natural Science Foundation of China (41604074, 41630209), and the China National Special Fund for Earthquake Scientific Research in Public Interest Science (201308011).

Appendix A. Supplementary material

Supplementary material related to this article can be found online at <https://doi.org/10.1016/j.epsl.2018.06.010>.

References

- Ammon, C.J., 1991. The isolation of receiver effects from teleseismic P waveforms. *Bull. Seismol. Soc. Am.* 81 (6), 2504–2510.
- Chang, L., Ding, Z., Wang, C., Flesch, L.M., 2017. Vertical coherence of deformation in lithosphere in the NE margin of the Tibetan Plateau using GPS and shear-wave splitting data. *Tectonophysics* 699, 93–101.
- Chen, J., Liu, Q., Li, S., Guo, B., Lai, W., 2005. Crust and upper mantle S-wave velocity structure across Northeastern Tibetan Plateau and Ordos block. *Chin. J. Geophys.* 48 (2), 333–342 (in Chinese).
- Chen, M., Huang, H., Yao, H., van der Hilst, R., Niu, F., 2014. Low wave speed zones in the crust beneath the SE Tibet revealed by ambient noise adjoint tomography. *Geophys. Res. Lett.* 41. <https://doi.org/10.1002/2013GL058476>.
- Chen, Y.L., Niu, F., Liu, R., Huang, Z., Tkalčić, H., 2010. Crustal structure beneath China from receiver function analysis. *J. Geophys. Res.* 115, B03307. <https://doi.org/10.1029/2009JB006386>.
- Chen, Y., Niu, F., 2013. Ray parameter based stacking and enhanced preconditioning for stable inversion of receiver function data. *Geophys. J. Int.* 194, 1682–1700.
- Christensen, N.I., 1996. Poisson's ratio and crustal seismology. *J. Geophys. Res.* 101, 3139–3156.
- Clark, M.K., Royden, L.H., 2000. Topographic ooze: building the eastern margin of Tibet by lower crustal flow. *Geology* 28, 703–706.
- Clayton, R.W., Wiggins, R., 1976. Source shape estimation and deconvolution of teleseismic body waves. *Geophys. J. R. Astron. Soc.* 47, 151–177.
- Crampin, S., Lovell, J., 1991. A decade of shear-wave splitting in the Earth's crust: what does it mean? What use can we make of it? and what should we do next? *Geophys. J. Int.* 107 (3), 387–407.

- Crampin, S., Peacock, S., 2008. A review of the current understanding of seismic shear-wave splitting in the Earth's crust and common fallacies in interpretation. *Wave Motion* 45, 675–722.
- Dewey, J.F., Shackleton, R., Chang, C., Sun, Y., 1988. The tectonic evolution of the Tibetan Plateau. *Philos. Trans. R. Soc. Lond. A* 327 (1594), 379–413.
- England, P., Houseman, G., 1986. Finite strain calculations of continental deformation: 2. Comparison with the India–Asia collision zone. *J. Geophys. Res.* 91 (3), 3664–3676.
- Erdman, M.E., Hacker, B.R., Zandt, G., Seward, G., 2013. Seismic anisotropy of the crust: electron-backscatter diffraction measurements from the basin and range. *Geophys. J. Int.* 195, 1211–1229.
- Guo, H., Ding, Z., Xu, X., 2017. Upper mantle structure beneath the northern South–North Seismic Zone from teleseismic traveltime data. *Chin. J. Geophys.* 60 (1), 86–97. <https://doi.org/10.6038/cjg20170108> (in Chinese).
- Hu, S., He, L., Wang, J., 2000. Heat flow in the continental area of China: a new data set. *Earth Planet. Sci. Lett.* 179 (2), 407–419.
- Huang, Z., Tilmann, F., Xu, M., Wang, L., Ding, Z., Mi, N., Yu, D., Li, H., 2017. Insight into NE Tibetan Plateau expansion from crustal and upper mantle anisotropy revealed by shear-wave splitting. *Earth Planet. Sci. Lett.* 478, 66–75.
- Kawakatsu, H., Niu, F., 1994. Seismic evidence for a 920-km discontinuity in the mantle. *Nature* 371, 301–305.
- Kennett, B., Engdahl, E., 1991. Travel times for global earthquake location and phase identification. *Geophys. J. Int.* 105, 429–465.
- Kreemer, C., Blewitt, G., Klein, E.C., 2014. A geodetic plate motion and Global Strain Rate Model. *Geochim. Geophys. Geosyst.* 15, 3849–3889. <https://doi.org/10.1002/2014GC005407>.
- Levin, V., Park, J., 1997. P-SH conversions in a flat-layered medium with anisotropy of arbitrary orientation. *Geophys. J. Int.* 131, 253–266.
- Li, H., Shen, Y., Huang, Z., Li, X., Gong, M., Shi, D., Sandvol, E., Li, A., 2014. The distribution of the mid-to-lower crustal low-velocity zone beneath the northeastern Tibetan Plateau revealed from ambient noise tomography. *J. Geophys. Res., Solid Earth* 119, 1954–1970. <https://doi.org/10.1002/2013JB010374>.
- Li, J., Wang, X., Niu, F., 2011. Seismic anisotropy and implications for mantle deformation beneath the NE margin of the Tibet plateau and Ordos plateau. *Phys. Earth Planet. Inter.* 189, 157–170. <https://doi.org/10.1016/j.pepi.2011.08.009>.
- Li, X., Santosh, M., Cheng, S., Xu, X., Zhong, W., 2015. Crustal structure and composition beneath the northeastern Tibetan Plateau from receiver function analysis. *Phys. Earth Planet. Inter.* 249, 51–58.
- Li, Y., Pan, J., Wu, Q., Ding, Z., 2017. Lithospheric structure beneath the northeastern Tibetan Plateau and the western Sino-Korea craton revealed by Rayleigh-wave tomography. *Geophys. J. Int.* 210 (2), 570–584. <https://doi.org/10.1093/gji/ggx181>.
- Liu, H., Niu, F., 2012. Estimating crustal seismic anisotropy with a joint analysis of radial and transverse receiver function data. *Geophys. J. Int.* 188, 144–164.
- Liu, Q.Y., van der Hilst, R., Li, Y., Yao, H., Chen, J., Guo, B., Qi, S., Wang, J., Huang, H., Li, S., 2014. Eastward expansion of the Tibetan plateau by crustal flow and strain partitioning across faults. *Nat. Geosci.* 7 (5), 361–365.
- Lowry, A., Pérez-Gussinyé, M., 2011. The role of crustal quartz in controlling Cordilleran deformation. *Nature* 471, 353–357.
- McNamara, D.E., Owens, T.J., 1993. Azimuthal shear wave velocity anisotropy in the Basin and Range Province using Moho Ps converted phases. *J. Geophys. Res.* 98 (B7), 12,003–12,017.
- Meissner, R., Mooney, W.D., Artemieva, I., 2002. Seismic anisotropy and mantle creep in young orogens. *Geophys. J. Int.* 149, 1–14.
- Meyer, B., Tapponnier, P., Bourjot, L., Metivier, F., Gadamer, Y., Peltzer, G., Shunmin, G., Zhitai, C., 1998. Crustal thickening in Gansu–Qinghai, lithospheric mantle subduction, and oblique, strike-slip controlled growth of the Tibet plateau. *Geophys. J. Int.* 135, 1–47. <https://doi.org/10.1046/j.1365-246X.1998.00567.x>.
- Molnar, P., Tapponnier, P., 1975. Cenozoic tectonics of Asia: effects of a continental collision. *Science* 189, 419–426.
- Muirhead, K.J., 1968. Eliminating false alarms when detecting seismic events automatically. *Nature* 217, 533–534.
- Niu, F., Kawakatsu, H., 1998. Determination of the absolute depths of the mantle transition zone discontinuities beneath China: effect of stagnant slabs on transition zone discontinuities. *Earth Planets Space* 50, 965–976.
- Niu, F., Li, J., 2011. Component azimuths of the CEArray stations estimated from P-wave particle motion. *Earthq. Sci.* 24, 3–13.
- Niu, F., Bravo, T., Gary, P., Vernon, F., Rendon, H., Bezada, M., Levander, A., 2007. Receiver function study of the crustal structure of the southeastern Caribbean plate boundary and Venezuela. *J. Geophys. Res.* 112 (B11). <https://doi.org/10.1029/2006JB004802>.
- Owens, T.J., Zandt, G., 1997. Implications of crustal property variations for models of Tibetan plateau evolution. *Nature* 387, 37–43.
- Pan, S., Niu, F., 2011. Large contrast in crustal structure and composition between the Ordos plateau and the NE Tibetan plateau from receiver function analysis. *Earth Planet. Sci. Lett.* 303, 291–298.
- Pandey, S., Yuan, X., Debayle, E., Tilmann, F., Priestley, K., Li, X., 2015. Depth-variant azimuthal anisotropy in Tibet revealed by surface wave tomography. *Geophys. Res. Lett.* 42 (11), 4326–4334.
- Qian, Q., Wu, J., Liu, G., Sha, C., Ma, J., Bai, Z., Zhao, Y., Liu, X., 2017. Anisotropy of middle-upper crust derived from shear-wave splitting in the northeastern Tibetan plateau and tectonic implications. *Chin. J. Geophys.* 60 (6), 2338–2349. <https://doi.org/10.6038/cjg20170625> (in Chinese).
- Rao, G., He, C., Cheng, Y., Yu, Y., Hu, J., Chen, P., Yao, Q., 2018. Active normal faulting along the Langshan Piedmont Fault, North China: implications for slip partitioning in the western Hetao Graben. *J. Geol.* 126, 99–118.
- Rost, S., Thomas, C., 2009. Improving seismic resolution through array processing techniques. *Surv. Geophys.* 30 (4–5), 271–299.
- Rowley, D.B., 1996. Age of initiation of collision between India and Asia: a review of stratigraphic data. *Earth Planet. Sci. Lett.* 145, 1–13.
- Royden, L.H., Burchfiel, B.C., van der Hilst, R.D., 2008. The geological evolution of the Tibetan plateau. *Science* 321, 1054–1058.
- Royden, L.H., Burchfiel, B.C., King, R.W., Wang, E., Chen, Z., Shen, F., Liu, Y., 1997. Surface deformation and lower crustal flow in eastern Tibet. *Science* 276, 788–790.
- Savage, M.K., 1998. Lower crustal anisotropy or dipping boundaries? Effects on receiver functions and a case study in New Zealand. *J. Geophys. Res.* 103, 15069–15087.
- Sherrington, H.F., Zandt, G., Frederiksen, A., 2004. Crustal fabric in the Tibetan Plateau based on waveform inversions for seismic anisotropy parameters. *J. Geophys. Res.* 109, B02312. <https://doi.org/10.1029/2002JB002345>.
- Shiomi, K., Park, J., 2008. Structural features of the subducting slab beneath the Kii Peninsula, central Japan: seismic evidence of slab segmentation, dehydration, and anisotropy. *J. Geophys. Res.* 113 (B10). <https://doi.org/10.1029/2007JB005535>.
- Silver, P.G., 1996. Seismic anisotropy beneath the continents: probing the depth of geology. *Annu. Rev. Earth Planet. Sci.* 24 (1), 385–432.
- Sun, Y., Niu, F., Liu, H., Chen, Y., Liu, J., 2012. Crustal structure and deformation of the SE Tibetan plateau revealed by receiver function data. *Earth Planet. Sci. Lett.* 349, 186–197.
- Tao, W., Shen, Z., 2008. Heat flow distribution in Chinese continent and its adjacent areas. *Prog. Nat. Sci.* 18, 843–849.
- Tapponnier, P., Xu, Z., Roger, F., Meyer, B., Arnaud, N., Wittlinger, G., Yang, J., 2001. Oblique stepwise rise and growth of the Tibet Plateau. *Science* 294, 1671–1677. <https://doi.org/10.1126/science.105978>.
- Tarkov, A.P., Vavakin, V.V., 1982. Poisson's ratio behaviour in crystalline rocks: application to the study of the Earth's interior. *Phys. Earth Planet. Inter.* 29, 24–29.
- Vinnik, L.P., 1977. Detection of waves converted from P to SV in the mantle. *Phys. Earth Planet. Inter.* 15, 39–45.
- Wang, Q., Niu, F., Gao, Y., Chen, Y., 2016. Crustal structure and deformation beneath the NE margin of the Tibetan Plateau constrained by teleseismic receiver function data. *Geophys. J. Int.* 204 (1), 167–179.
- Wang, W., Wu, J., Fang, L., Lai, G., Cai, Y., 2017a. Sedimentary and crustal thicknesses and Poisson's ratios for the NE Tibetan Plateau and its adjacent regions based on dense seismic arrays. *Earth Planet. Sci. Lett.* 462, 76–85.
- Wang, X., Li, Y., Ding, Z., Zhu, L., Wang, C., Bao, X., Wu, Y., 2017b. Three-dimensional lithospheric S wave velocity model of the NE Tibetan Plateau and western North China Craton. *J. Geophys. Res., Solid Earth* 122, 6703–6720. <https://doi.org/10.1002/2017JB014203>.
- Watson, M.P., Hayward, A.B., Parkinson, D.N., Zhang, Z.M., 1987. Plate tectonic history, basin development and petroleum source rock deposition onshore China. *Mar. Pet. Geol.* 4, 205–225.
- Wu, C., Yin, A., Zuza, A., Zhang, J., Liu, W., Ding, L., 2016. Pre-Cenozoic geologic history of the central and Northern Tibetan Plateau and the role of Wilson cycles in constructing the Tethyan orogenic system. *Lithosphere* 8 (3), 254–292.
- Xie, Z., Wu, Q., Zhang, R., 2017. Crustal anisotropy beneath northeastern margin of the Tibetan plateau and its dynamic implications. *Chin. J. Geophys.* 60 (6), 2315–2325 (in Chinese).
- Xu, X.M., Ding, Z., Shi, D., Li, X., 2013. Receiver function analysis of crustal structure beneath the eastern Tibetan plateau. *J. Asian Earth Sci.* 73, 121–127.
- Yang, Y., Ritzwoller, M.H., Zheng, Y., Shen, W., Levshin, A., Xie, Z., 2012. A synoptic view of the distribution and connectivity of the mid-crustal low velocity zone beneath Tibet. *J. Geophys. Res.* 117, B04303. <https://doi.org/10.1029/2011JB008810>.
- Yao, H., Beghein, C., van der Hilst, R., 2008. Surface wave array tomography in SE Tibet from ambient seismic noise and two-station analysis – II. Crustal and upper-mantle structure. *Geophys. J. Int.* 173, 205–219.
- Ye, Z., Gao, R., Li, Q., Zhang, H., Shen, X., Liu, X., Gong, C., 2015. Seismic evidence for the North China plate underthrusting beneath northeastern Tibet and its implications for plateau growth. *Earth Planet. Sci. Lett.* 426, 109–127.
- Ye, Z., Li, Q., Gao, R., Zhang, H., Shen, X., Liu, X., Gong, C., 2016. Anisotropic regime across northeastern Tibet and its geodynamic implications. *Tectonophysics* 671, 1–8.
- Yin, A., Harrison, T.M., 2000. Geologic evolution of the Himalayan–Tibetan orogeny. *Annu. Rev. Earth Planet. Sci.* 28, 211–280.
- Yue, H., et al., 2012. Lithospheric and upper mantle structure of the northeastern Tibetan Plateau. *J. Geophys. Res.* 117, B05307. <https://doi.org/10.1029/2011JB008545>.
- Zandt, G., Ammon, C., 1995. Continental crust composition constrained by measurements of crustal Poisson's ratio. *Nature* 374, 152–154.

- Zhang, H., Gao, Y., Shi, Y., Liu, X., Wang, Y., 2012a. Tectonic stress analysis based on the crustal seismic anisotropy in the northeastern margin of Tibetan plateau. *Chin. J. Geophys.* 55 (1), 95–104 (in Chinese).
- Zhang, H., Teng, J., Tian, X., Zhang, Z., Gao, R., Liu, J., 2012b. Lithospheric thickness and upper-mantle deformation beneath the NE Tibetan Plateau inferred from S receiver functions and SKS splitting measurements. *Geophys. J. Int.* 191, 1285–1294. <https://doi.org/10.1111/j.1365-246X.2012.05667.x>.
- Zhang, Y.Q., Mercier, J.L., Vergly, P., 1998. Extension in the rift systems around the Ordos (China), and its contribution to the extrusion tectonics of south China with respect to Gobi-Mongolia. *Tectonophysics* 285 (1), 41–75.
- Zhao, B., Huang, Y., Zhang, C., Wang, W., Tan, K., Du, R., 2015. Crustal deformation on the Chinese mainland during 1998–2014 based on GPS data. *Geodesy Geodyn.* 6, 7–15. <https://doi.org/10.1016/j.geog.2014.12.006>.
- Zhao, D., Isozaki, Y., Maruyama, S., 2017. Seismic imaging of the Asian orogens and subduction zones. *J. Asian Earth Sci.* 145, 349–367.
- Zheng, D., Li, H., Shen, Y., Tan, J., Ouyang, L., Li, X., 2016. Crustal and upper mantle structure beneath the northeastern Tibetan Plateau from joint analysis of receiver functions and Rayleigh wave dispersions. *Geophys. J. Int.* 204 (1), 583–590.
- Zuza, A.V., Cheng, X., Yin, A., 2016. Testing models of Tibetan Plateau formation with Cenozoic shortening estimates across the Qilian Shan–Nan Shan thrust belt. *Geosphere* 12 (2), 1–32. <https://doi.org/10.1130/GES01254.1>.